

PCA-Enhanced Adaptive NVAR Framework for High-Resolution Sea Surface Temperature Forecasting in the East Sea

Sherkhon Azimov^{a,*}, Susana López-Moreno^{a,b,c}, Eric Dolores-Cuenca^{b,d}, JinYong Choi^e, Sangil Kim^{a,f,*}

^aDepartment of Mathematics, Pusan National University, Republic of Korea

^bHumanoid Olfactory Display Center, Pusan National University, Republic of Korea

^cIndustrial Mathematics Center, Pusan National University, Republic of Korea

^dDepartment of Mathematics, Yonsei University, Republic of Korea

^eMarine Natural Disaster Research Department, Korea Institute of Ocean Science and Technology, Republic of Korea

^fInstitute for Future Earth, Pusan National University, Republic of Korea

Abstract

Accurate forecasting of sea surface temperature (SST) in regional seas such as the East Sea is crucial for monitoring marine ecosystems, assessing climate risks, managing fisheries, and conducting naval operations. Traditional numerical ocean models provide reliable predictions but are computationally expensive and often unsuitable for real-time forecasting. Many deep learning methods also struggle with high-dimensional spatiotemporal ocean data and experience error accumulation over longer forecasting periods. This study builds on our previously proposed Adaptive Next-Generation Reservoir Computing (Adaptive NVAR) framework, initially introduced and tested on synthetic dynamical systems, and extends it to ocean forecasting. We present a reduced-order forecasting framework that combines Singular Value Decomposition (SVD) with Adaptive NVAR to predict SST dynamics in the East Sea. SST fields are compressed into a low-dimensional representation using SVD, which extracts dominant modes of ocean variability. Adaptive NVAR models the temporal evolution of these latent states, and the predicted states are reconstructed into SST forecasts. We evaluate the framework using regional ocean datasets and compare it with the standard NG-RC/NVAR. Results show that Adaptive NVAR consistently achieves lower forecasting errors across multiple prediction horizons. In addition, SVD reduces computational complexity, resulting in a fast and scalable framework suitable for real-time ocean forecasting.

Keywords: sea surface temperature forecasting, NVAR, dynamical systems

1. Introduction

Accurate forecasting of high-resolution Sea Surface Temperature (SST) in regional domains, such as the East Sea, is crucial for monitoring marine ecosystems, assessing climate risks, managing fisheries, and supporting naval operations [1, 2]. The East Sea serves as a unique regional natural laboratory, marked by a highly dynamic, multi-scale upper-layer circulation system [3]. Traditional numerical ocean circulation models provide physically consistent and reliable predictions. However, their immense computational demands render them impractical for real-time operational forecasting or large-scale ensemble simulations.

To overcome these computational bottlenecks, data-driven approaches and machine learning frameworks have emerged as powerful alternatives. While deep learning techniques show great potential, they frequently encounter significant challenges when applied to complex, high-dimensional spatiotemporal ocean data. These limitations include rapid error accumulation during long-term autoregressive rollouts, a profound lack of physical interpretability, and prohibitive training costs.

In a fast-changing region like the East Sea, these forecasting challenges become even worse. The basin serves as a complex mixing zone where strong, warm ocean currents, such as the northward-moving East

*Corresponding authors

Email addresses: sherxonazimov94@pusan.ac.kr (Sherkhon Azimov), sangil.kim@pusan.ac.kr (Sangil Kim)

Korea Warm Current, collide with cold northern currents. This interaction creates a sharp and constantly shifting Subpolar Front [4, 5]. The collision results in a turbulent environment filled with swirling water patterns and chaotic mesoscale eddies [6]. When unpredictable atmospheric conditions frequently disrupt this shallow ocean surface layer, they leave behind complex variations that act as an unstable memory [7]. For standard machine learning models, trying to predict through this chaotic mix over long time periods leads to significant and unstable error accumulation.

Recently, Next-Generation Reservoir Computing (NG-RC), also widely referred to as the standard Non-linear Vector Autoregression (standard NVAR) framework, has gained considerable attention as a stable and efficient paradigm for modeling complex dynamical systems [8]. By leveraging time-delay embeddings and fixed polynomial feature mappings, standard NVAR eliminates the need for expensive recurrent network training while preserving the structural advantages of traditional Reservoir Computing (RC). Comparative studies on chaotic time series have demonstrated that RC techniques can match or even exceed the trajectory-tracking accuracy of Recurrent Neural Networks (RNNs) and Long Short-Term Memory (LSTM) while offering dramatically lower computational overhead and avoiding gradient-based training anomalies [9]. Despite these benefits, standard NVAR can struggle when deployed on highly nonstationary geophysical processes, where fixed, predetermined feature mappings fail to capture evolving nonlinear interactions over extended periods.

To address these limitations, the Adaptive NVAR framework was recently introduced [10]. As a data-adaptive nonlinear vector autoregressive model, it utilizes a trainable Multi-Layer Perceptron (MLP) to learn optimal nonlinear feature representations directly from data. This modification drastically improves scalability and performance under high-dimensional, noisy, and complex conditions compared to standard NVAR, Echo State Networks (ESNs), and hybrid ESN architectures, all while preserving a lightweight and elegant structure. The competitive edge of this approach was recently highlighted by Ren et al. [11] in their development of the Dynamic Causal-Temporal Forecasting Model (DCTFM); when benchmarked against an Adaptive NVAR configuration, the two models yielded highly competitive performance results, with Adaptive NVAR achieving remarkably close accuracy despite its significantly simpler architecture and lower number of parameters.

This study builds directly upon these advancements, extending the application of the Adaptive NVAR framework from low-dimensional synthetic chaotic benchmarks to real-world geophysical forecasting challenges. To handle the high spatial dimensionality inherent to oceanographic fields, we present a unified spatiotemporal forecasting framework that merges Singular Value Decomposition (SVD)—analogous to spatial Principal Component Analysis (PCA)—with the Adaptive NVAR model to predict high-resolution SST dynamics in the East Sea.

The structure of our proposed approach is as follows:

- **Dimensionality Reduction:** High-resolution spatial SST fields are compressed into a lower dimensional space using SVD to identify the main empirical orthogonal functions that influence regional ocean dynamics.
- **Latent-Space Dynamics Modeling:** We model the temporal changes of these latent states using the Adaptive NVAR framework. This framework uses a multi-layer perceptron (MLP) to learn optimal nonlinear feature representations dynamically instead of depending on static polynomial combinations.
- **Spatiotemporal Reconstruction:** We map the predicted latent trajectories back to the original spatial domain using an inverse PCA transformation, resulting in full-resolution, multi-step-ahead spatial SST forecasts.

We assess the performance of our framework by using the high-resolution Copernicus Marine Service Global Ocean Physics Reanalysis (GLORYS12V1) dataset [12] over a defined area in the East Sea. Our results show that the Adaptive NVAR model consistently outperforms standard NVAR/NG-RC setups. It achieves significantly lower error metrics across various forecasting periods of up to 90 days. Additionally, incorporating SVD-based dimensionality reduction significantly reduces the computational requirements. This creates a scalable and fast framework ideal for real-time oceanographic applications.

The rest of this paper is organized as follows: Section 2 explains the theoretical basis of the standard and adaptive NVAR frameworks along with the dimensionality reduction process. Section 3 describes the numerical experiments, dataset features, hyperparameter tuning, and forecasting results. Finally, Section 4 illustrates the conclusions of the paper and explores directions for future research.

2. Methodology

2.1. Spatiotemporal Dimensionality Reduction via Singular Value Decomposition

To efficiently model high-dimensional geophysical fields, we use a principal component analysis (PCA) based on the SVD to map the spatial data into a low-dimensional, orthogonal latent space [13]. Edward Lorenz was one of the first to introduce this mathematical tool to atmospheric and climate science [14]. Let $\mathbf{U} \in \mathbb{R}^{M \times T}$ represent the spatiotemporal data matrix. Here, M is the total number of spatial grid points on a surface layer, and T is the number of temporal snapshots. The full SVD of the data matrix is expressed as:

$$\mathbf{U} = \mathbf{\Phi} \mathbf{\Sigma} \mathbf{V}^\top,$$

where $\mathbf{\Phi} \in \mathbb{R}^{M \times M}$ contains the orthogonal spatial eigenvectors (empirical orthogonal functions, or EOFs), $\mathbf{\Sigma} \in \mathbb{R}^{M \times T}$ is a rectangular diagonal matrix containing the singular values in descending order, and $\mathbf{V} \in \mathbb{R}^{T \times T}$ represents the temporal coefficients.

While large climate datasets with significant dimensions often need probabilistic, randomized SVD methods [15] to prevent memory issues, the smaller spatial scale of the East Sea area allowed us to perform a complete, exact deterministic decomposition. To simplify the structure and remove high-frequency spatial noise, we create a low-dimensional approximation by truncating the expansion to the first r dominant modes ($r \ll M$):

$$\mathbf{U} \approx \mathbf{\Phi}_r \mathbf{\Sigma}_r \mathbf{V}_r^\top = \mathbf{\Phi}_r \mathbf{Z},$$

where $\mathbf{\Phi}_r \in \mathbb{R}^{M \times r}$ denotes the truncated spatial basis matrix, and $\mathbf{Z} = \mathbf{\Sigma}_r \mathbf{V}_r^\top \in \mathbb{R}^{r \times T}$ represents the reduced-order temporal state trajectories. The mathematical optimality of this low-rank approximation is guaranteed by the Eckart-Young-Mirsky theorem [16], which proves that the truncated SVD minimizes the reconstruction error in terms of both the Frobenius and spectral matrix norms. The matrix \mathbf{Z} serves as the direct low-dimensional input time series \mathbf{u}_t for both the standard NVAR baseline (Section 2.2) and the proposed Adaptive NVAR framework (Section 2.3). Following autoregressive state prediction in the latent space, the physical fields are reconstructed via linear combination with the preserved spatial modes:

$$\hat{\mathbf{u}}_{t+1}^{\text{physical}} = \mathbf{\Phi}_r \hat{\mathbf{u}}_{t+1}.$$

2.2. Next-Generation Reservoir Computing

The standard nonlinear vector autoregression (NVAR) framework, serving as the core mathematical formulation for Next-Generation Reservoir Computing (NG-RC) [8], completely replaces the random, recurrent internal spaces of traditional reservoir networks with an explicit, deterministic spatiotemporal feature mapping. Let $\mathbf{u}_t \in \mathbb{R}^d$ represent the d -dimensional input vector at time step t . The total NVAR feature vector \mathbf{O}_t is constructed via concatenation:

$$\mathbf{O}_t = c \oplus \mathbf{O}_t^{\text{lin}} \oplus \mathbf{O}_t^{\text{nonlin}},$$

where c is a constant scalar bias term and \oplus denotes vector concatenation. The delay-embedded linear feature vector $\mathbf{O}_t^{\text{lin}}$ at time step t is explicitly structured as [17]:

$$\mathbf{O}_t^{\text{lin}} = \mathbf{u}_t \oplus \mathbf{u}_{t-\tau} \oplus \mathbf{u}_{t-2\tau} \oplus \cdots \oplus \mathbf{u}_{t-(k-1)\tau},$$

where k is the delay embedding length parameter and τ is the delay stride spacing. Consequently, the linear feature vector $\mathbf{O}_t^{\text{lin}}$ spans a total dimension of $k \cdot d$.

A core structural advantage of this formulation over traditional recurrent architectures is that NVAR does not require an extended warm-up (or washout) period to clear transient initial states; it requires exactly

$k_s = (k - 1)\tau + 1$ historical steps to establish its operational feature space [8]. For simplicity and structural consistency across models, we set $\tau = 1$ for all NVAR variations evaluated in this work.

The nonlinear feature component $\mathbf{O}_t^{\text{nonlin}}$ is built directly from the unique elements of the linear delay vector. Following the standard NG-RC convention [8], a polynomial quadratic expansion is applied, meaning $\mathbf{O}_t^{\text{nonlin}}$ contains all unique second-order monomials formed from the elements of $\mathbf{O}_t^{\text{lin}}$:

$$\mathbf{O}_t^{\text{nonlin}} = \mathbb{V}(\mathbf{O}_t^{\text{lin}} \otimes \mathbf{O}_t^{\text{lin}}),$$

where \otimes denotes the vector outer product and $\mathbb{V}(\cdot)$ extracts the $N_{\text{nonlin}} = \frac{1}{2}(kd)(kd + 1)$ unique, non-redundant terms.

The optimization of the NVAR framework utilizes a Tikhonov regularized least-squares cost function, resulting in the closed-form formulation [18]:

$$\mathbf{W}_{\text{out}} = \mathbf{Y}\mathbf{O}^\top (\mathbf{O}\mathbf{O}^\top + \lambda\mathbf{I})^{-1},$$

where \mathbf{O} is the assembled feature matrix across all training points, $\lambda > 0$ is the regularization parameter, and \mathbf{I} is the identity matrix. Following [8], the target labels are formulated as forward operational differences, $\mathbf{Y}_t = \mathbf{u}_{t+1} - \mathbf{u}_t$, yielding an Euler-like integration rollout rule for the autoregressive forecasting:

$$\hat{\mathbf{Y}}_t = \mathbf{W}_{\text{out}}\mathbf{O}_t. \quad (1)$$

This difference-based target is preserved across all variations to ensure comparative consistency. A schematic representation of the standard NVAR pipeline is illustrated in Figure 1.

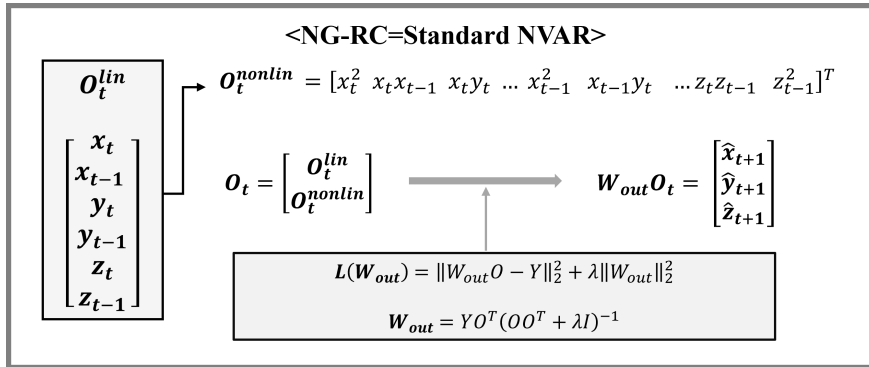


Figure 1: Schematic representation of the Next-Generation Reservoir Computing (or standard NVAR) framework showing deterministic delay embedding and polynomial feature generation.

2.3. Adaptive Nonlinear Autoregressive Model

While standard NVAR and Adaptive NVAR share an identical linear delay-embedding vector $\mathbf{O}_t^{\text{lin}}$ and an incremental Euler prediction rule, they differ fundamentally in how their nonlinear feature spaces are formed and optimized.

Instead of relying on hardcoded, static polynomial features, Adaptive NVAR handles complex spatiotemporal structures by modeling nonlinear feature spaces using a shallow, trainable multi-layer perceptron (MLP) [10]. Leveraging the properties of neural networks as universal function approximators [19], we introduce a parameterized mapping $\phi_{\Theta} : \mathbb{R}^{kd} \rightarrow \mathbb{R}^m$ that transforms the delay embedding space dynamically:

$$\mathbf{O}_t^{\text{nonlin}} = \phi_{\Theta}(\mathbf{O}_t^{\text{lin}}),$$

where Θ denotes the total set of learnable network weights and biases, and m specifies the output feature dimensionality produced by the network. In practice, this neural mapping is realized via a shallow MLP architecture formulated as:

$$\phi_{\Theta}(\mathbf{O}_t^{\text{lin}}) = \sigma(\mathbf{W}_2 \cdot \sigma(\mathbf{W}_1 \mathbf{O}_t^{\text{lin}} + \mathbf{b}_1) + \mathbf{b}_2), \quad (2)$$

where $\mathbf{W}_1, \mathbf{W}_2, \mathbf{b}_1, \mathbf{b}_2 \in \Theta$ represent the trainable structural parameters, and $\sigma(\cdot)$ denotes an element-wise nonlinear activation function.

The resulting total feature space is formed by concatenating the original linear delay-embedded vector directly with the learned nonlinear representation via an explicit structural skip connection:

$$\mathbf{O}_t^{\text{total}} = \mathbf{O}_t^{\text{lin}} \oplus \mathbf{O}_t^{\text{nonlin}}. \quad (3)$$

Note that an explicit constant bias term is omitted from (3), since bias vectors are implicitly handled within the neural network parameters Θ .

The temporal rollout update uses a linear readout layer that operates over the combined feature space to predict the state increment, matching the target structure in (1):

$$\hat{\mathbf{Y}}_t = \mathbf{W}_{\text{out}} \mathbf{O}_t^{\text{total}} = \mathbf{W}_{\text{out}} (\mathbf{O}_t^{\text{lin}} \oplus \phi_{\Theta} (\mathbf{O}_t^{\text{lin}})).$$

The operational flow of this skip-connection-based forward pass is detailed systematically in Algorithm 1.

Algorithm 1 Adaptive NVAR Forward Pass Execution

Require: Linear delay-embedded trajectory vector $\mathbf{O}_t^{\text{lin}}$

Ensure: Predicted state increments $\hat{\mathbf{Y}}_t$

- 1: **Parameters:** Trainable neural mapping parameters Θ , readout weights \mathbf{W}_{out}
 - 2: **Nonlinear Feature Generation:** Compute $\mathbf{O}_t^{\text{nonlin}} \leftarrow \phi_{\Theta} (\mathbf{O}_t^{\text{lin}})$ via (2)
 - 3: **Skip-Connection:** Form combined feature space $\mathbf{O}_t^{\text{total}} \leftarrow \mathbf{O}_t^{\text{lin}} \oplus \mathbf{O}_t^{\text{nonlin}}$
 - 4: **Readout Evaluation:** Compute predicted increment $\hat{\mathbf{y}}_t \leftarrow \mathbf{W}_{\text{out}} \mathbf{O}_t^{\text{total}}$
 - 5: **return** $\hat{\mathbf{y}}_t$
-

Unlike standard configurations that rely on static matrix inversions, Adaptive NVAR trains its parameters end-to-end. The linear readout weights \mathbf{W}_{out} and internal network parameters Θ are optimized jointly using a gradient-based optimization procedure that minimizes the mean squared error over the valid training indices:

$$\mathcal{L}_{\text{Adaptive}} = \frac{1}{N_{\text{samples}}} \sum_{t=k_s}^T \|\mathbf{W}_{\text{out}} (\mathbf{O}_t^{\text{lin}} \oplus \phi_{\Theta} (\mathbf{O}_t^{\text{lin}})) - \mathbf{Y}_t\|_2^2,$$

where $\mathbf{Y}_t = \mathbf{u}_{t+1} - \mathbf{u}_t$ is the true observed state increment matrix and N_{samples} is the total number of training steps. This joint optimization forces the extracted nonlinear features to adapt dynamically to the true underlying system trajectories, eliminating the need for fixed hand-engineered feature matrices and improving stability over long horizons. An overview of the proposed framework is shown in Figure 2.

3. Numerical experiments

3.1. Dataset description

This study uses the Copernicus Marine Service Global Ocean Physics Reanalysis dataset, known as GLORYS12V1 [12]. This dataset provides high-resolution global ocean reanalysis fields created with the NEMO ocean circulation model and includes several observational sources. The GLORYS12V1 dataset has a horizontal spatial resolution of $1/12^\circ$ (about 8 km) with 50 vertical ocean levels. It provides daily oceanographic variables starting from 1993. This study only used the SST variable at the surface layer (0.49m) for forecasting experiments. The dataset was restricted to the East Sea using these geographic boundaries: latitude from 35°N to 39°N , and longitude from 129.8°E to 132°E . A total of 5000 daily sea surface temperature samples were collected from August 19, 2012, to April 27, 2026. The last day snapshot is shown in Figure 3.

The extracted regional SST fields have dimensions (5000, 1, 49, 27) corresponding to 5001 temporal snapshots, 1 surface depth level, 49 latitude grid points, and 27 longitude grid points. For the tested

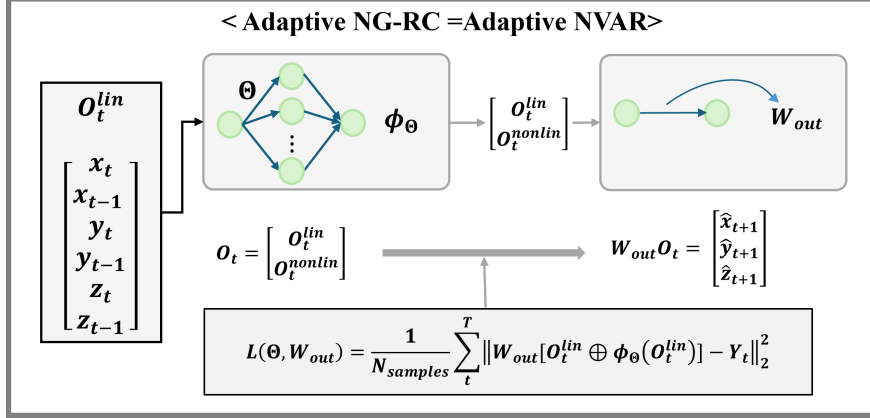


Figure 2: Schematic representation of the Adaptive NVAR framework showcasing the learnable MLP nonlinear mapping and the unified skip-connection optimization architecture.

models, the spatial SST fields were reshaped into a two-dimensional matrix before dimensionality reduction and forecasting. Specifically, the SST tensor was flattened along the spatial dimensions:

$$X \in \mathbb{R}^{5000 \times 1323},$$

where each time step is represented by a $49 \times 27 = 1323$ -dimensional spatial feature vector. This representation was later used for the PCA-enhanced modeling and the forecasting models.

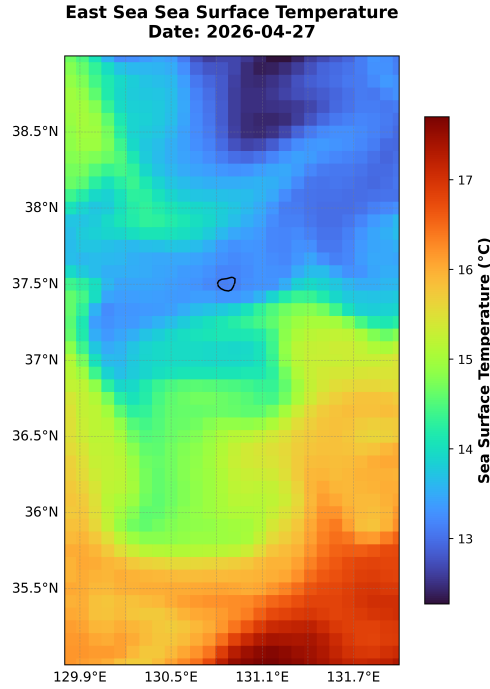


Figure 3: Sample SST snapshot from the Copernicus Marine GLORYS12V1 reanalysis dataset used in this study

All data were obtained in NetCDF-4 format from the Copernicus Marine Service platform.

3.2. Dimensionality Reduction of SST Data

The original SST dataset has 5,000 time samples and 1,323 spatial grid points, forming a data matrix of shape (5,000, 1,323). To reduce the complexity of the SST field while also keeping its main variability, we used PCA through the full SVD algorithm. We computed the PCA decomposition using only the training portion of the dataset to prevent information leakage from the validation and testing datasets. Specifically, we fitted the PCA basis using SST snapshots from the warm-up and training period, corresponding to the first 4,000 samples. After fitting the PCA basis, we projected the complete SST dataset onto the low-dimensional subspace formed by the training PCA modes. We kept a truncated representation with $n_{\text{comp}} = 1$ principal component.

Table 1 and Figure 4 show that the first principal component captures approximately 97.08% of the total variance, shown by the explained variance ratio $\lambda_1 \approx 0.97083$. The first 10 components collectively explain more than 99% of the variance, indicating that the SST dynamics are low-dimensional.

We then used the one-dimensional latent representation as the dynamical state variable for both the standard NVAR and Adaptive NVAR forecasting models. Finally, we obtained the reconstructed SST fields by applying the inverse PCA transformation to the predicted latent trajectories.

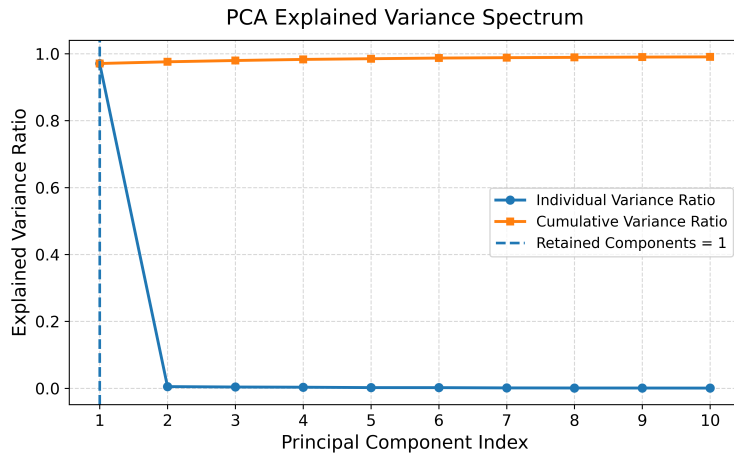


Figure 4: Explained variance spectrum of the PCA decomposition computed from the SST training dataset. The cumulative explained variance exceeds 99% within the first 10 principal components.

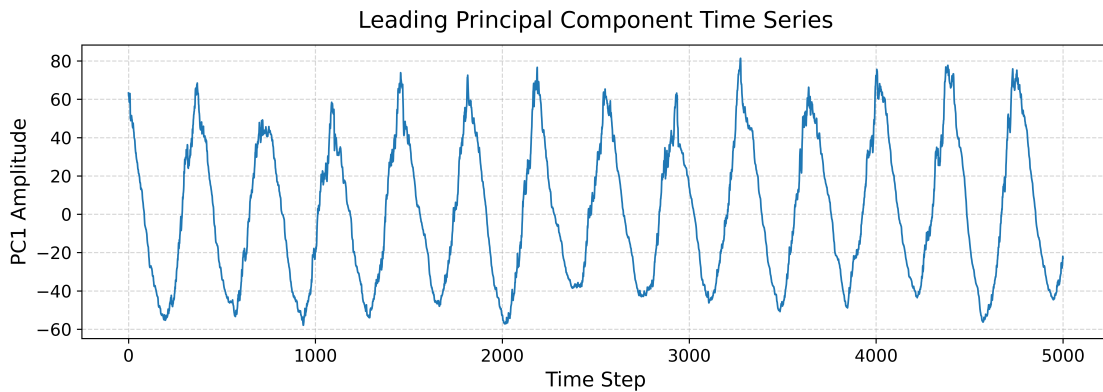


Figure 5: Temporal evolution of the leading principal component (PC_1) obtained from the PCA decomposition.

Figure 5 shows the temporal evolution of the leading (first) principal component, which represents the dominant large-scale SST variability captured by the SVD.

Table 1: Explained variance ratios of the leading PCA modes computed from the SST training dataset.

| Principal Component | Explained Variance Ratio | Cumulative Variance Ratio |
|---------------------|--------------------------|---------------------------|
| PC1 | 0.970823 | 0.970823 |
| PC2 | 0.005084 | 0.975907 |
| PC3 | 0.003847 | 0.979754 |
| PC4 | 0.003261 | 0.983015 |
| PC5 | 0.002088 | 0.985103 |
| PC6 | 0.001977 | 0.987080 |
| PC7 | 0.001182 | 0.988262 |
| PC8 | 0.000907 | 0.989169 |
| PC9 | 0.000809 | 0.989978 |
| PC10 | 0.000626 | 0.990605 |

3.3. Training procedure

The dataset was divided into training, validation, and testing subsets. The total data length was divided into four sequential segments consisting of a warm-up + training period, validation period, and testing period using an 80/10/10 temporal splitting strategy. Specifically, the warm-up duration was set to 100 time samples, the training duration to 3900 samples, the validation duration to 500 samples, and the testing duration to 500 samples. To evaluate the models' performance, we conducted forecasting at 10, 30, 60, and 90-step (day) intervals.

Let $y_{i,t}$ denote the true value of the i -th variable at time step t , and $\hat{y}_{i,t}$ denote the corresponding prediction. Assume N is the number of variables and T is the forecast horizon (number of time steps). We measured the model's performance using three common error metrics: the mean squared error (MSE), defined as

$$\text{MSE} = \frac{1}{NT} \sum_{i=1}^N \sum_{t=1}^T (y_{i,t} - \hat{y}_{i,t})^2,$$

the mean absolute error (MAE), defined as

$$\text{MAE} = \frac{1}{NT} \sum_{i=1}^N \sum_{t=1}^T |y_{i,t} - \hat{y}_{i,t}|,$$

and the root mean squared error (RMSE), computed as

$$\text{RMSE} = \sqrt{\frac{1}{NT} \sum_{i=1}^N \sum_{t=1}^T (y_{i,t} - \hat{y}_{i,t})^2}.$$

For rolling-window evaluation, the final reported metric is obtained by averaging the error values across all forecast windows. If W denotes the total number of rolling windows and $\text{MSE}^{(w)}$ denotes the MSE of the w -th window, then the average rolling-window MSE is

$$\overline{\text{MSE}} = \frac{1}{W} \sum_{w=1}^W \text{MSE}^{(w)}.$$

Similarly, the average rolling-window MAE and RMSE are given by

$$\overline{\text{MAE}} = \frac{1}{W} \sum_{w=1}^W \text{MAE}^{(w)}$$

and

$$\overline{\text{RMSE}} = \frac{1}{W} \sum_{w=1}^W \text{RMSE}^{(w)}.$$

The model was first pretrained using the Adam optimizer [20] for fast convergence and stable parameter initialization. It was then fine-tuned using the L-BFGS optimizer [21], which is effective for small-dimensional models such as adaptive NVAR.

3.4. Hyperparameter search

Table 2 summarizes the hyperparameter search spaces used for optimizing the Tree-structured Parzen Estimator (TPE) [22, 23] for the standard NVAR and Adaptive NVAR models. The optimization process examined the delay embedding dimension and model-specific training parameters across wide logarithmic and discrete search ranges. Table 3 shows the best hyperparameter settings found through TPE optimization along with the corresponding optimization times. Adaptive NVAR took longer to optimize because of the extra neural network-related hyperparameters. The validation and test evaluation were done using overlapping rolling forecast windows. Each window had a size of 90 time steps and a stride of 1. This approach led to a total of 411 autonomous forecasting windows across both datasets.

Table 2: Hyperparameter search ranges used in the TPE optimization method.

| Hyperparameter | Search Range |
|--------------------------------|---------------------------|
| <i>Standard NVAR</i> | |
| Delay embedding length k | $k \in \{1, \dots, 50\}$ |
| Ridge regularization λ | $10^{-8} - 10^5$ |
| <i>Adaptive NVAR</i> | |
| Delay embedding length k | $k \in \{1, \dots, 50\}$ |
| Number of hidden units in MLP | $\{10, 20, 30, 50, 100\}$ |
| Initial Adam learning rate | $10^{-5} - 10^{-1}$ |
| Initial L-BFGS learning rate | $10^{-3} - 10^0$ |

Table 3: Optimal hyperparameter configurations and optimization time obtained using TPE optimization.

| Hyperparameter | Optimal Value | Optimization Time |
|--------------------------------|-----------------------|-------------------|
| <i>Standard NVAR</i> | | |
| Delay embedding length k | 46 | 33 min 54 sec |
| Ridge regularization λ | 1.99×10^5 | |
| <i>Adaptive NVAR</i> | | |
| Delay embedding length k | 26 | 48 min 11 sec |
| Number of hidden units | 20 | |
| Adam learning rate | 1.36×10^{-5} | |
| L-BFGS learning rate | 4.57×10^{-1} | |

3.5. Experimental results

Table 4 summarizes the forecasting performance of the standard NVAR and Adaptive NVAR models on the reconstructed SST fields using the TEST dataset. We evaluated forecast accuracy over forecasting horizons of 10, 30, 60, and 90 days.

Table 4: Horizon-wise reconstructed SST forecast errors for standard NVAR and Adaptive NVAR models on the test dataset. Best results for each metric are indicated with bold letters.

| Horizon | Standard NVAR | | | Adaptive NVAR | | |
|---------|---------------|----------|----------|-----------------|-----------------|-----------------|
| | MSE | MAE | RMSE | MSE | MAE | RMSE |
| 10 | 0.043029 | 0.162932 | 0.207434 | 0.041713 | 0.161804 | 0.204238 |
| 30 | 0.065804 | 0.198411 | 0.256523 | 0.059593 | 0.193020 | 0.244118 |
| 60 | 0.123365 | 0.263321 | 0.351233 | 0.090809 | 0.240857 | 0.301345 |
| 90 | 0.209092 | 0.336655 | 0.457266 | 0.117524 | 0.273058 | 0.342818 |

Both models showed increasing forecast errors as the prediction horizon got longer. This is expected because of the buildup of errors in autoregressive predictions during long-term rollout. However, Adaptive NVAR consistently outperformed the standard NVAR model at all forecasting horizons and error metrics.

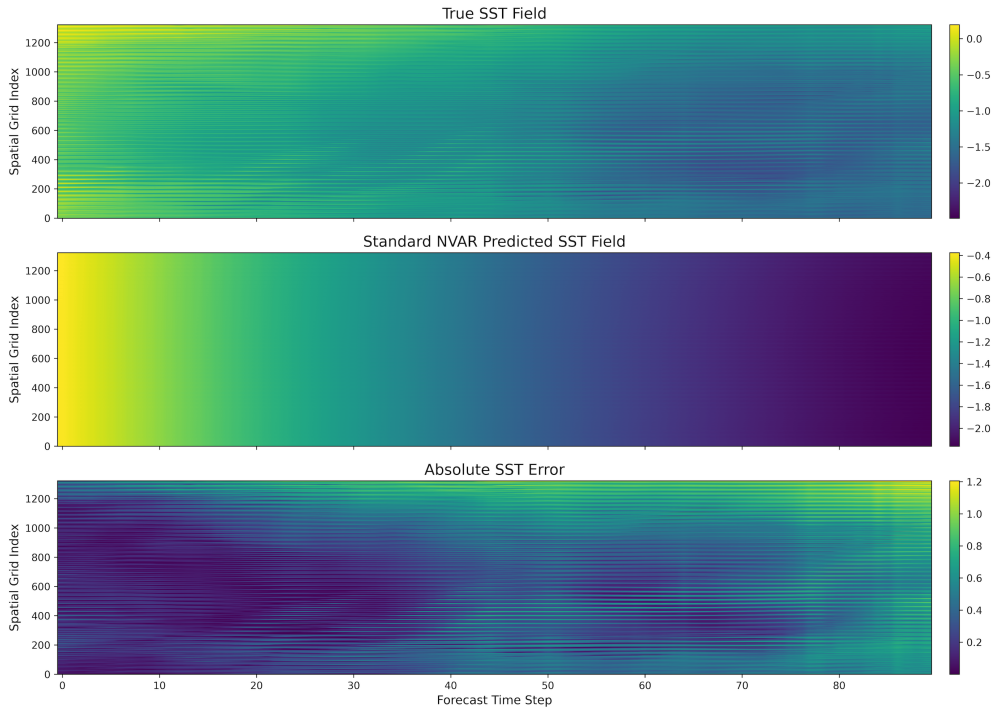


Figure 6: Comparison between the true SST field, the SST field reconstructed by the standard NVAR model, and the corresponding absolute prediction error over the forecasting horizon.

At the short-term horizon of 10 days, both models had relatively low reconstruction errors. Adaptive NVAR had a slightly better performance, with an RMSE of 0.204238, compared to 0.207434 for the standard NVAR model.

The performance gap widened as the forecast horizon increased. At the 60 day horizon, Adaptive NVAR reduced the SST RMSE from 0.351233 to 0.301345, which is about a 14.2% improvement. At the longest horizon of 90 steps, Adaptive NVAR achieved an RMSE of 0.342818, which is significantly lower than the

0.457266 of the standard NVAR model. This reflects an approximate RMSE reduction of 25.0%. The MSE and MAE metrics showed similar trends, further supporting Adaptive NVAR’s stronger long-term forecasting ability.

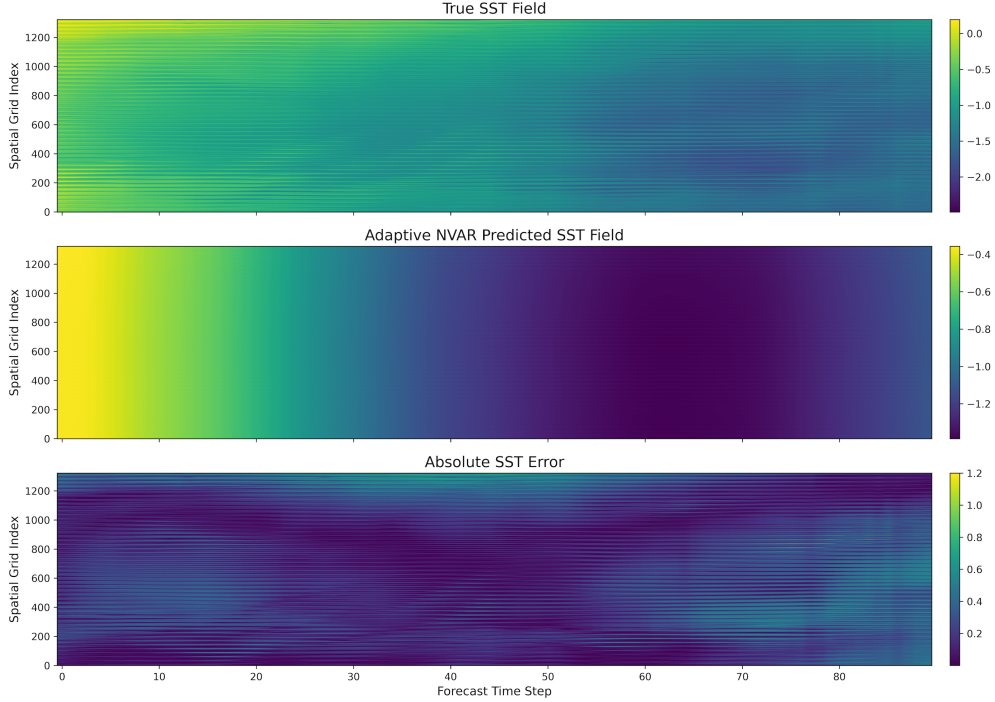


Figure 7: Comparison between the true SST field, the SST field reconstructed by the proposed Adaptive NVAR model, and the corresponding absolute prediction error over the forecasting horizon.

Figures 6 and 7 compare the SST field reconstruction performance of the standard NVAR and the Adaptive NVAR frameworks. Both models capture the main large-scale spatiotemporal evolution of the SST dynamics during the forecasting period. However, clear differences appear in their long-term reconstruction behavior and error accumulation patterns.

In Figure 6, the standard NVAR model shows increasing reconstruction error as the forecasting horizon extends. The predicted SST field becomes smoother and diverges from the reference SST dynamics at later forecast steps. The absolute error field reveals significant error growth across many spatial areas, especially during the later stages of autoregressive prediction. This pattern suggests that the standard NVAR framework accumulates more long-term errors and has less stability in recreating fine-scale SST variability.

In contrast, Figure 7 demonstrates that the proposed Adaptive NVAR model maintains much better reconstruction stability throughout the same forecasting period. The predicted SST field effectively preserves the dominant temporal evolution and the large-scale spatial structures while showing slower error growth over time. Although some smoothing of fine-scale spatial variability occurs due to the reduced-order SVD representation, the overall absolute error magnitude is considerably lower and more spatially coherent compared to the standard NVAR model.

4. Conclusion

In this study, we looked into autonomous SST forecasting using standard NVAR and Adaptive NVAR model in a reduced latent space created by PCA. The dimensionality reduction kept the main SST variability

while making the forecasting task much simpler. The first principal component captured over 97% of the total variance.

The experimental results revealed that both models could produce stable autonomous forecasts over various prediction horizons. However, the adaptive NVAR consistently performed better than the standard NVAR across all evaluation measures, including MSE, MAE, and RMSE. The performance improvement was more visible at longer forecast horizons. This showed that the adaptive nonlinear feature representation reduced error buildup and improved long-term forecasting stability.

The reconstructed SST field analyses further indicated that Adaptive NVAR was better at preserving the underlying spatiotemporal SST patterns during the autonomous rollout. These findings suggest that adding adaptive nonlinear feature learning to the NVAR framework helps the model capture the complex nonlinear ocean dynamics more effectively than using fixed quadratic feature mappings.

This work points out the potential of adaptive NVAR models as efficient alternatives for long-term climate and ocean forecasting tasks. Unlike many large-scale deep learning methods, the proposed framework delivers strong forecasting results while keeping a relatively simple and semi-interpretable structure. This makes it appealing for scientific forecasting applications where efficiency and stability matter.

Future research will aim to expand the framework to higher-dimensional latent representations and include additional physical constraints. It will also focus on reconstructing forecasts directly on the original spatial SST grids.

Computational Environment

All experiments and analyses were conducted using the Jupyter Notebook [24]. All computations were performed on the system configuration summarized in Table 5. The main libraries used in this study were Matplotlib [25] for visualization, NumPy [26] and SciPy [27] for numerical computations, Optuna [22] for hyperparameter search, and PyTorch [28] for implementing the models.

Table 5: Runtime environment used for the experiments.

| Name | Configuration |
|------------------|--|
| CPU | Intel(R) Xeon(R) Gold 6242 CPU @ 2.80GHz |
| GPU | NVIDIA A100-PCIE-40GB |
| Memory | 376.54 GB RAM |
| Operating System | Linux 3.10.0-1062.el7.x86_64 (64-bit) |

Code Availability

The source code used in this study is available from the corresponding author upon request.

Acknowledgments

This work was supported by a National Research Foundation of Korea (NRF) grant funded by the Korean Government (MSIT) (2022R1A5A1033624; RS-2023-00242528); the Global Learning & Academic Research Institution for Master’s, Ph.D. students, and Postdocs (LAMP) Program of the National Research Foundation of Korea (NRF) grant, funded by the Ministry of Education (No. RS-2023-00301938); the Korea Institute of Marine Science & Technology Promotion (KIMST) funded by the Ministry of Oceans and Fisheries, Korea (RS-2025-02217872); and the Glocal University 30 Project at Pusan National University through the Institute for Regional System & Education in Busan Metropolitan City, funded by the Ministry of Education(MOE) and the Busan Metropolitan City, Republic of Korea.(2025-glocal-02-004-M432-09).

Additionally, the work of S. López-Moreno was supported by the Korea National Research Foundation (NRF) grant funded by the Korean government (MSIT) (RS-2024-00406152), and the work of E. Dolores Cuenca was supported by the Korea National Research Foundation (NRF) grant funded by the Korean government (MSIT) (RS-2025-00517727).

Correspondence

Correspondence and requests for materials should be addressed to Sangil Kim (email: sangil.kim@pusan.ac.kr) and Sherkhon Azimov (email: sherxonazimov94@pusan.ac.kr).

References

- [1] H.-J. Ju, J.-Y. Chae, E.-J. Lee *et al.*, “Impacts of seasonal and interannual variabilities of sea surface temperature on its short-term deep-learning prediction model around the southern coast of korea,” *The Sea Journal of the Korean Society of Oceanography*, vol. 27, no. 2, pp. 49–70, 2022.
- [2] X. Zhang, Y. Li, A. C. Frery *et al.*, “Sea surface temperature prediction with memory graph convolutional networks,” *IEEE Geoscience and Remote Sensing Letters*, vol. 19, pp. 1–5, 2021.
- [3] C. N. Mooers, H. Kang, I. Bang *et al.*, “Some lessons learned from comparisons of numerical simulations and observations of the jes circulation,” *Oceanography*, vol. 19, no. 3, pp. 86–95, 2006.
- [4] T. Kim and J.-H. Yoon, “Seasonal variation of upper layer circulation in the northern part of the east/japan sea,” *Continental shelf research*, vol. 30, no. 12, pp. 1283–1301, 2010.
- [5] C. M. Lee, L. N. Thomas, and Y. Yoshikawa, “Intermediate water formation: at the japan/east sea subpolar front,” *Oceanography*, vol. 19, no. 3, pp. 110–121, 2006.
- [6] O. Trusenkova, V. Lobanov, and D. Kaplunenko, “Dynamically induced anomalies of the japan/east sea surface temperature,” *Ocean and Polar Research*, vol. 31, no. 1, pp. 11–29, 2009.
- [7] G. Lim and J.-J. Park, “Winter sea-surface-temperature memory in the east/japan sea under the arctic oscillation: Time-integrated forcing, coupled hot spots, and predictability windows,” *Remote Sensing*, vol. 18, no. 1, p. 79, 2025.
- [8] D. J. Gauthier, E. Bollt, A. Griffith *et al.*, “Next generation reservoir computing,” *Nature communications*, vol. 12, no. 1, p. 5564, 2021.
- [9] S. Shahi, F. H. Fenton, and E. M. Cherry, “Prediction of chaotic time series using recurrent neural networks and reservoir computing techniques: A comparative study,” *Machine learning with applications*, vol. 8, p. 100300, 2022.
- [10] A. Sherkhon, S. Lopez-Moreno, E. Dolores-Cuenca *et al.*, “Adaptive nonlinear vector autoregression: Robust forecasting for noisy chaotic time series,” *arXiv preprint arXiv:2507.08738*, 2025.
- [11] W. Ren, M. Gao, H. Ma *et al.*, “Dctfm: A dynamic causal-temporal forecasting model for marine data,” *Ocean Engineering*, vol. 358, p. 125733, 2026.
- [12] L. Jean-Michel, G. Eric, B.-B. Romain *et al.*, “The copernicus global 1/12 oceanic and sea ice glorys12 reanalysis,” *Frontiers in Earth Science*, vol. 9, p. 698876, 2021.
- [13] A. Hannachi, I. T. Jolliffe, D. B. Stephenson *et al.*, “Empirical orthogonal functions and related techniques in atmospheric science: A review,” *International journal of climatology*, vol. 27, no. 9, pp. 1119–1152, 2007.

- [14] E. N. Lorenz *et al.*, *Empirical orthogonal functions and statistical weather prediction*. Massachusetts Institute of Technology, Department of Meteorology Cambridge, 1956, vol. 1.
- [15] N. Halko, P.-G. Martinsson, and J. A. Tropp, “Finding structure with randomness: Probabilistic algorithms for constructing approximate matrix decompositions,” *SIAM review*, vol. 53, no. 2, pp. 217–288, 2011.
- [16] C. Eckart and G. Young, “The approximation of one matrix by another of lower rank,” *Psychometrika*, vol. 1, no. 3, pp. 211–218, 1936.
- [17] H. Kantz and T. Schreiber, *Nonlinear time series analysis*. Cambridge university press, 2003.
- [18] A. N. Tikhonov, “Solutions of ill posed problems,” 1977.
- [19] K. Hornik, M. Stinchcombe, and H. White, “Multilayer feedforward networks are universal approximators,” *Neural networks*, vol. 2, no. 5, pp. 359–366, 1989.
- [20] D. P. Kingma and J. Ba, “Adam: A method for stochastic optimization,” in *3rd International Conference on Learning Representations, ICLR 2015, San Diego, CA, USA, May 7-9, 2015, Conference Track Proceedings*, Y. Bengio and Y. LeCun, Eds., 2015. [Online]. Available: <http://arxiv.org/abs/1412.6980>
- [21] D. C. Liu and J. Nocedal, “On the limited memory bfgs method for large scale optimization,” *Mathematical programming*, vol. 45, no. 1, pp. 503–528, 1989.
- [22] T. Akiba, S. Sano, T. Yanase *et al.*, “Optuna: A next-generation hyperparameter optimization framework,” in *Proceedings of the 25th ACM SIGKDD international conference on knowledge discovery & data mining*, 2019, pp. 2623–2631.
- [23] J. Bergstra, R. Bardenet, Y. Bengio *et al.*, “Algorithms for hyper-parameter optimization,” *Advances in neural information processing systems*, vol. 24, 2011.
- [24] T. Kluyver, B. Ragan-Kelley, F. Pérez *et al.*, “Jupyter notebooks – a publishing format for reproducible computational workflows,” in *Positioning and Power in Academic Publishing: Players, Agents and Agendas*, F. Loizides and B. Schmidt, Eds. IOS Press, 2016, pp. 87 – 90.
- [25] J. Hunter and D. Dale, “The matplotlib user’s guide,” *Matplotlib 0.90. 0 user’s guide*, vol. 487, 2007.
- [26] C. R. Harris, K. J. Millman, S. J. van der Walt *et al.*, “Array programming with NumPy,” *Nature*, vol. 585, no. 7825, pp. 357–362, Sep. 2020. [Online]. Available: <https://doi.org/10.1038/s41586-020-2649-2>
- [27] P. Virtanen, R. Gommers, T. E. Oliphant *et al.*, “SciPy 1.0: Fundamental Algorithms for Scientific Computing in Python,” *Nature Methods*, vol. 17, pp. 261–272, 2020.
- [28] A. Paszke, S. Gross, S. Chintala *et al.*, “Automatic differentiation in pytorch,” 2017.